Dynamics of Cellular Retinoic Acid Binding Protein I on Multiple Time Scales with Implications for Ligand Binding[†]

V. V. Krishnan,*[‡] Muppalla Sukumar,[§,||] Lila M. Gierasch,[§] and Monique Cosman[‡]

Biology and Biotechnology Research Program, Lawrence Livermore National Laboratory, 7000 East Avenue, L-448 Livermore, California 94551, and Department of Chemistry, University of Massachusetts, Amherst, Massachusetts 01003

Received February 8, 2000; Revised Manuscript Received May 17, 2000

ABSTRACT: Cellular retinoic acid binding protein I (CRABPI) belongs to the family of intracellular lipid binding proteins (iLBPs), all of which bind a hydrophobic ligand within an internal cavity. The structures of several iLBPs reveal minimal structural differences between the apo (ligand-free) and holo (ligand-bound) forms, suggesting that dynamics must play an important role in the ligand recognition and binding processes. Here, a variety of nuclear magnetic resonance (NMR) spectroscopy methods were used to systematically study the dynamics of both apo and holo CRABPI at various time scales. Translational and rotational diffusion constant measurements were used to study the overall motions of the proteins. Both apo and holo forms of CRABPI tend to self-associate at high (1.2 mM) concentrations, while at low concentrations (0.2 mM), they are predominantly monomeric. Rapid amide exchange rate and laboratory frame relaxation rate measurements at two spectrometer field strengths (500 and 600 MHz) were used to probe the internal motions of the individual residues. Several residues in the apo form, notably within the ligand recognition region, exhibit millisecond time scale motions that are significantly arrested in the holo form. In contrast, no significant differences in the high-frequency motions were observed between the two forms. These results provide direct experimental evidence for dynamics-induced ligand recognition and binding at a specifically defined time scale. They also exemplify the importance of dynamics in providing a more comprehensive understanding of how a protein functions.

Cellular retinoic acid binding protein I (CRABPI)[1] (136 residues, 15.5 kDa) is a member of the intracellular lipid binding protein (iLBP) family (*1*−*5*) which contains 17 additional members (*4*, *5*), including the recently discovered *Manduca sexta* CRABP (msCRABP) (*6*). These proteins are expressed in diverse cell types ranging from epithelial to neural (*7*), and bind hydrophobic ligands such as fatty acids, lipids, and retinoids. Each protein in this family exhibits high specificity for its respective ligand with binding constants in the nanomolar range (*8*−*10*). CRABPI specifically transports retinoic acid (RA), an active metabolite of vitamin A (retinol), which mediates several vitamin A-dependent processes in the cell (*11*). Although the exact role of CRABPI in the cell is not known, its differential distribution in chick limb buds suggests that it is indirectly involved in spatial modulation of gene transcription (*7*, *12*).

The structures of 11 iLBPs have been determined by either X-ray crystallography or NMR spectroscopy (*5*) and show a high degree of structural homology, with CRABPII being the closest homologue to CRABPI. The conservation of the backbone structures among these proteins is remarkable, with root-mean-square (rms) deviations between the α-carbon positions ranging from 0.63 to 2.38 Å (*4*). All the structures determined consist of two five-stranded, antiparallel orthogonal *β*-sheets (*β*-strands designated A−J), and a short N-terminal helix (αI)−turn−helix (αII). The *β*-sheets face one another to form a sandwich commonly termed a *β*-clam, the interior of which contains the ligand-binding cavity. The inner surface of the cavity is lined with both hydrophilic and hydrophobic amino acids. The volume of the cavity is larger than the combined volume of the bound ligand and crytallographically observed solvent molecules (*4*). Although a gap 6−12 Å wide is present between the D and E *β*-strands, the side chains from these strands are interleaved and prevent free access to the central cavity. Comparison of the apo (without ligand) and holo (with bound ligand) structures of proteins in this family shows that ligand binding does not induce any large conformational change (*4*).

Since the relative arrangement of the *β*-strands and αI−turn−αII blocks access to the binding cavity, several hypotheses have been proposed to describe possible mechanisms by which the ligand can enter or exit. In one model, it is proposed that the high flexibility of the αI−turn−αII region of the protein, which is highly conserved in the iLBPs,

---

[†] Research by M.S. and L.M.G. was supported by NIH Grant GM27616. This work was performed under the auspices of the U.S. Department of Energy by the Lawrence Livermore National Laboratory under Contract W-7405-ENG-48 and supported by Lawrence Livermore National Laboratory LDRD Director's Initiative Grants 96-DI-010 and 99-LW-031.

* To whom correspondence should be addressed. E-mail: krish@llnl.gov.

[‡] Lawrence Livermore National Laboratory.

[§] University of Massachusetts.

[||] Current address: Eli Lilly and Company, Indianapolis, IN 46285.

[1] Abbreviations: CRABPI, cellular retinoic acid binding protein I; NMR, nuclear magnetic resonance; NOE, nuclear Overhauser effect; iLBP, intracellular lipid binding protein; WEXII-FHSQC, water exchange II fast heteronuclear single-quantum correlation; PDB, Protein Data Bank; BPP-SED, bipolar pulsed field gradient selective echo dephasing; SASA, solvent accessible surface area; rms, root-mean-square; NOESY, nuclear Overhauser effect spectroscopy; TOCSY, total correlation spectroscopy.

10.1021/bi000296l CCC: $19.00

plays an important role in identifying and allowing the correct ligand to enter the binding pocket and bind with high affinity (*13*, *14*). On the basis of the packing density of atoms on the surface in the crystal structures of intestinal fatty acid binding protein (IFABP), Sacchettini et al. (*13*) identified a small opening in the region enclosed by αI, αII, and turns between βC−βD and βE−βF. This region was designated as a "portal" or door that regulates ligand recognition and binding. This "portal hypothesis" was extended to the "dynamic portal hypothesis" by Hodson and Cistola (*15*, *16*) on the basis of the amide backbone relaxation and the exchange behavior of the same protein. In this model, the residues in the portal region are able to exhibit large movements that enable the opening or closing of the portal. Since a narrow channel is observed in this region, it has also been suggested that motions in this region can widen this crevice to accommodate ligand entry without resorting to large motions. Moreover, electrostatic potentials appear to play a part in ligand recruitment since the crevice and the binding pocket are lined with positively charged residues (*17*, *18*). It has also been suggested that an order−disorder transition occurs upon ligand binding and that release of the ligand might occur due to collisional mechanisms (*15*). A recent crystallographic study of the mutant of the apo CRABPII (R111M) (*18*, *19*) suggests that partial unwinding of αII assists the opening of the portal, in addition to conformational mobility of the Arg residues in the loop regions between βC−βD and βE−βF.

Another model for ligand recognition and binding is based on the 2.7 Å crystal structure of the apo CRABPI (*20*). In this model, transfer of bound ligand to another protein molecule occurs through protein−protein association or oligomerization, such as formation of dimers. However, NMR studies of CRABPII (R111M) (*18*, *19*, *21*) argue against the formation of dimers in solution for this close homologue (77% identical sequence) of CRABPI and support conformational flexibility as an acceptable mechanism for ligand entry.

The lack of conformational differences between the apo and holo structures and the inaccessibility of the ligand-binding pocket suggest that dynamics of the iLBPs must play a critical role in the recognition and binding of their respective ligands (*4*, *5*, *10*, *19*, *22*−*26*). Thus, to shed further light on the ligand recognition problem, several NMR experiments were carried out to identify any differences in dynamic behavior between the apo and holo forms. Translational self-diffusion coefficient measurements show the presence of higher oligomeric states such as dimers at high (1.2 mM) concentrations. At a lower protein concentration (0.2 mM), where the protein is predominantly monomeric, a detailed analysis of rapid water−amide proton exchange rate measurements showed that the largest difference between the apo and holo forms involves motions that occur on the millisecond time scale. Laboratory frame relaxation rates, heteronuclear NOE experiments at two spectrometer field strengths, and analysis of data using reduced spectral density mapping showed that other higher-frequency motions are not significantly different between the apo and holo forms.

MATERIALS AND METHODS

Sample Preparation. Expression and purification of uniformly ^{15}N-labeled recombinant CRABPI were carried out as previously described (*14*). The protein eluted from the last ion exchange chromatography step was dialyzed extensively against water, which was adjusted to pH 7.5 with a small amount of liquid ammonia. The dialyzed sample was lyophilized and stored at −80 °C. NMR samples were prepared by dissolving the protein in 10 mM potassium phosphate (pH 7.5), 5 mM β-metcaptoethanol, 10% D_2O, and 0.03% sodium azide (NMR buffer) to a concentration of 0.2 or 1.2 mM, based on the absorbance at 280 nm (extinction coefficient of 21 294 cm^{-1} M^{-1}). Holo CRABP was prepared by adding a slight molar excess (1.2-fold) of concentrated retinoic acid in DMSO to a dilute solution (1 mg/mL) of protein. The total concentration of DMSO was kept below 1.5% v/v. The sample was concentrated by ultrafiltration in a Centricon tube and exchanged with NMR buffer to remove excess free retinoic acid. The stoichiometry of CRABP to retinoic acid in the final sample was close to 1:1 based on the ratio of absorbance to extinction coefficient at 280 and 350 nm, respectively. Samples for NMR experiments were thoroughly degassed under vacuum with gentle stirring for 10−15 min in a Pyrex glass tube. Part of the sample (600 μL) was then transferred to NMR tubes which were flushed with helium and capped.

NMR Spectroscopy. All experiments were carried out at 25 °C using either a Varian 600 MHz *INOVA* ($B_o = 14.1$ T) spectrometer or a Bruker AMX-500 MHz ($B_o = 11.7$ T) spectrometer, as indicated. Self-diffusion coefficients were measured in a triple-axes pulsed field gradient probe that is actively shielded, while all the other experiments were performed in indirect detection probe, with a single-axis (along z) actively shielded gradient coil. The probe temperature was calibrated using an external methanol reference. The gradient strength was calibrated with reference to the self-diffusion coefficient of residual H_2O (1.87×10^{-9} m^2 s^{-1} at 25 °C) in doped D_2O (0.1 mg/mL $GdCl_3$).

Self-Diffusion Coefficient Measurements. Self-diffusion coefficient measurements were obtained using the BPP-SED (bipolar pulsed field gradient selective echo dephasing) sequence (*27*−*29*) at 600 MHz. The experimental parameters were as follows: acquisition time, 0.328 s; spectral width, 12 500 Hz; signal averaging, 64 and 256 scans for the high- and low-concentration samples, respectively; recycling delay, 4 s; and water-selective pulse, 4 ms. Other delays are as follows: $\tau = 0.1$ ms, $\delta/2 = 7$ ms, and $T = 130$ ms. Gradients were varied from 1 to 32 G cm^{-1} in units of 0.5 G cm^{-1}, while the other gradients were applied at a strength of 30 G cm^{-1} for 1 ms each, yielding a total echo time ($\tau_1 + \tau_2$) of 14.026 ms. Phase cycling was used to advantageously utilize the radiation damping effects for water suppression as previously reported (*28*).

Calculation and Estimation of Diffusion Constants. Isotropic values of the self-diffusion coefficient (D_s^{calc}) and rotational correlation times (τ_c^{calc}) were estimated from their respective translational and rotational diffusion tensor, based on the beads model approximation of García de la Torre and Bloomfield (*30*). In this method, the protein is modeled as a collection of point sources of friction (denoted as beads) with hydrodynamic Oseen tensor interactions between them. The diffusion tensors are calculated from a set of linear equations solved by integrating the $3N \times 3N$ matrix, where N is the number of atoms determined from the structure of the protein. The program DIFFC based on the beads theory was used in the present work (*31*). All backbone atoms were considered as beads of equal size, where σ (bead radius) = 5.0 Å, at 25 °C, and the viscosity (in newtons per square meter) of pure water at the same temperature was used.

The empirical relationship between rotational correlation time (τ_c) and solvent accessible surface area (SASA), eq 1 proposed by Krishnan and Cosman (*32*), was used to determine theoretical τ_c values:

$$\mathrm{SASA} = K_r(\rho)\tau_c^{\ 2/3} \qquad (1)$$

where $K_r(\rho)$ is the theoretical or experimental empirical value given by 2031.8 ± 26.5 or 1775.9 ± 45.9 $m^2\ s^{-(2/3)}$, respectively. In these analyses, SASA and τ_c are in units of square angstroms and nanoseconds, respectively. SASA was calculated using the three-dimensional structures of apo and holo CRABPI (PDB access codes 1cbi and 1cbr, respectively) using Quanta (Molecular Simulations Inc.) with a probe ratio of 1.4 Å and a surface point density of 20.

Rapid Amide Exchange Rate Measurements. Rapid amide exchange rates were measured using the WEX II FHSQC pulse sequence (*33*) at 600 MHz. The WEXII part of the sequence is used to transfer magnetization from the water spins to the amide protons for a specified mixing time (τ_{mix}), and then the decay is monitored by a ^{1}H-detected fast HSQC experiment. The sequence was modified to detect rapidly exchanging amide protons by using a continuous gradient throughout the mixing time (gradients G_1 and G_2 in the original sequence). Gradient pulses (duration of 500 μs) at a strength of 0.4 G cm^{-1} were applied at 1 ms intervals. A total of eight mixing times were used (τ_{mix} = 0, 6.6, 12.0, 21.0, 30.9, 41.7, 52.5, and 71.4 ms) with duplicates at 0 and 71.4 ms. The spectral widths used for all the experiments were 10 000 and 2500 Hz for the ^{1}H and ^{15}N dimensions, respectively. Two hundred fifty-six and 64 transients were used for the low- and high-concentration samples, respectively, with a recycling delay of 2 s. The acquisition times along the t_2 and t_1 dimensions were 51 and 12.8 ms, respectively, for each complex point, while States−TPPI was used for quadrature detection in the indirect dimension. ^{15}N hard pulses were applied at a field strength of 10.2 kHz, while the decoupling was achieved by the multi-pulse sequence GARP1 (*34*) at 1.5 kHz. Water magnetization at the beginning of the sequence was selected using a single lobe *sinc* [sin(x)/x]-shaped pulse.

Laboratory Frame Relaxation Experiments. The ^{15}N longitudinal and transverse relaxation rate constants, R_1 and R_2, respectively, were determined by collecting a time series of two-dimensional ^{1}H−^{15}N correlation spectra with an appropriate Rance−Kay type of sensitivity enhancement (*35*−*37*).

R_1^{500} and R_2^{500} data sets were obtained using relaxation delays of 8, 16, 24, 40, 56, 80, 112, 152, and 200 ms for R_2 experiments and 10, 60.2, 140.4, 240.7, 361, 531.5, 752.1, and 1143.2 ms for R_1 experiments with duplicate measurements at all the time points. ^{15}N hard pulses were applied at a field strength of 6.4 kHz, while the decoupling during acquisition was achieved with a WALTZ-16 sequence (*38*) at 1.9 kHz. {^{1}H}−^{15}N steady-state NOE data sets were obtained by acquiring spectra with and without ^{1}H saturation prior to the beginning of the experiment. ^{1}H saturation was achieved by a series of 120° pulses (at a field strength of 7.5 kHz) applied 5 ms apart for a total of 3 s (*39*). A total of 64 or 128 transients were collected for each complex data point for R_1, R_2, and NOE measurements for the low- or high-concentration samples, while the recycling delays between the transients were 1.5, 1.5, and 5 s, respectively. Spectral widths of 4273.5 and 2000 Hz were used in the direct (^{1}H) and indirect dimensions (^{15}N), respectively, with acquisition times of 239.6 and 50 ms, respectively.

Relaxation delays for the R_1^{600} and R_2^{600} data sets were chosen on the basis of the optimal sampling methods provided by Jones et al. that is based on the Cramer−Rao invariance approach (*40*, *41*). From the initial estimates of the average values of T_1 (ca. $\langle T_1\rangle_{av} = 1/\langle R_1\rangle_{av}$ = 850 ms) and T_2 (ca. $\langle T_2\rangle_{av} = 1/\langle R_2\rangle_{av}$ = 50 ms) obtained at 500 MHz, a linear sampling scheme was selected to sample relaxation delays. A total of eight points were sampled for R_1^{600} and R_2^{600} at 0, 245.25, 490.50, 730.3, 975.55, 1220.8, 1460.6, and 1711.3 ms and at 0.0, 14.4, 28.89, 43.34, 57.79, 72.24, 86.68, and 101.13 ms, respectively, with duplicate measurements performed only at the first and last sampling points. Field strengths for the ^{15}N pulses were the same as in the rapid amide exchange rate measurements. {^{1}H}−^{15}N steady-state NOE data sets were collected in the same manner as that of the data at 500 MHz, with the field strength for the ^{1}H saturation pulses applied at 7.5 kHz. Signal averaging for the low- and high-concentration samples was obtained over 256 and 64 transients, respectively, with the delay between the transients for the R_1 (R_2) and NOE experiments being 1.5 s (3 s). The acquisition times along the t_2 (^{1}H) and t_1 (^{15}N) dimensions are 102 and 14.2 ms, respectively, while the spectral widths in the corresponding dimensions were 10 000 and 2250 Hz, respectively. In all the experiments described above, the carrier for the proton frequency was kept on the water resonance and the referencing in both the dimensions was performed externally using the standard methods.

Data Processing and Analysis. Data obtained at 600 MHz (14.1 T) were processed using NMRPipe (*42*). Rapid amide exchange rates (R_1 and R_2) and heteronuclear NOE time domain data along t_1 were forward linear predicted once before application of a combination of cosine bell and a weak Lorentzian−Gaussian function, and only a cosine apodization was applied along the t_2 dimension. The data were zero-filled once before Fourier transformation. The software package NMRView (*43*) was used for peak picking and calculation of peak intensities. R_1, R_2, and heteronuclear NOE time domain data obtained at 500 MHz (11.7 T) were processed on a Silicon Graphics workstation using Felix version 95 (MSI Inc., San Diego, CA). For each time domain data set, Gaussian and shifted sine bell apodization were applied along the t_2 and t_1 dimensions, respectively. All the spectra were zero-filled once prior to Fourier transformation followed by a zero-order baseline correction along the ω_2 dimension. Individual peak heights were measured from the spectra using Felix macros (courtesy of M. Akke, Lund University, Lund, Sweden). The uncertainties in the peak heights were estimated from the duplicated experiments or from the base plane noise. R_1^{500} and R_2^{500} rate constants were calculated using SigmaPlot, while R_1^{600} and R_2^{600} were calculated using Fortran codes developed in-house. Relaxation rate constants and related uncertainties were determined by fitting the experimental points to a monoexponential function. Heteronuclear steady-state NOEs were determined as the ratio of the peak intensities with and without proton saturation.

Time domain self-diffusion coefficient data were zero-filled once, and a cosine bell apodization was applied prior to complex Fourier transformation. The area under each spectrum from 4.25 to −1 ppm was integrated, and a nonlinear least-squares fit of eq 2 was used to estimate the self-diffusion coefficients (*27*).

$$S(q) = S(0)\exp[-D_s q^2(\Delta - \delta/3 - \tau/2)] \qquad (2)$$

$S(q)$ is the measured integral value as a function of q, and $S(0)$ is the value at $q = 0$. q is the effective area of the gradient pulse given by ($\gamma g_z \delta$), where γ is the gyromagnetic ratio of proton (2.6752×10^8 s^{-1} T^{-1}) and g_z and δ are the amplitude and duration of the gradient pulse, respectively. D_s is given in units of square meters per second, while Δ and τ are delays employed in the pulse sequence in seconds.

Rapid amide exchange rates (k_{ex}^{HH}) were determined on the basis of the procedure outlined by Mori et al. (*33*, *44*). The rate of transfer of magnetization from the water to the amide protons is given by

$$I(\tau_{mix}) = [k_{ex}^{HH}/(R_{1w} + k_{ex}^{HH} - R_{1NH})] \times \{\exp(-R_{1NH}\tau_{mix}) - \exp[-(R_{1w} + k_{ex}^{HH})\tau_{mix}]\} \qquad (3)$$

where $I(\tau_{mix})$ is the normalized cross-peak intensity with respect to the zero-mixing time experiment, τ_{mix} is the mixing time, and R_{1w} and R_{1NH} are the spin−lattice relaxation rates of water and amide protons, respectively. R_{1w} was estimated by independent measurements to be 0.28 s^{-1}. To minimize cross-relaxation contributions, a two-parameter fit of $I(\tau_{mix})$ was performed to estimate k_{ex}^{HH}. The intensity of each of the amide cross-peaks was normalized with respect to their intensity in the experiment collected with a mixing time of zero.

Reduced Spectral Density Mapping. For a heteronuclear two-unlike spin system, the relaxation rate constants (R_1 and R_2) and the steady-state heteronuclear NOE between the ^{1}H−^{15}N spin pair can be given by the power spectral density functions of the rotational motions (*45*, *46*) at five frequencies ($\omega = 0$, ω_N, $\omega_H - \omega_N$, ω_H, and $\omega_H + \omega_N$). In the reduced spectral density mapping approach (*47*, *48*), assuming that $dJ(\omega)/d\omega^2$ is relatively constant between the linear combinations $\omega_H + \omega_N$ and $\omega_H - \omega_N$, the rate constants and NOE can be expressed as a linear combination of only three spectral density functions, $J(0)$, $J(\omega_N)$, and $J(0.87\omega_H)$ (*47*−*49*). Following this procedure, the spectral density functions at these three frequencies in terms of the relaxation parameters can be written as

$$J(0) = (6R_2 - 3R_1 - 2.72\sigma)/(3d^2 + 4c^2) \qquad (4)$$

$$J(\omega_N) = (4R_1 - 5\sigma)/(3d^3 + 4c^2) \qquad (5)$$

$$J(0.87\omega_H) = 4\sigma/5d^2 \qquad (6)$$

where σ [=(NOE − 1)$R_1\gamma_N/\gamma_H$] is the cross relaxation rate of the spin pair and γ_H and γ_N are the gyromagnetic ratios of the ^{1}H and ^{15}N nuclei, respectively. Accurate estimation of $J(0)$ values is complicated because the measured R_2 values are sensitive to motions on the millisecond to microsecond time scale. These motions tend to increase the apparent values of $J(0)$ and may yield unreliable estimates of $J(0)$ in some cases. As the contributions of these motions to the effective line width increase with the square of the spectrometer frequency, measurements at two field strengths (500 and 600 MHz) allow the determination of reliable effective spectral density values close to the zero frequency $J_{eff}(0)$ and the contributions from millisecond scale motions, R_{ex} (*49*):

$$J_{eff}(0) = 1/\beta\{(R_2^{600} - \kappa R_2^{500}) - (3d^2/8)[J(\omega_N^{600}) - \kappa J(\omega_N^{500})] - (c^2_{600}/2)[J(\omega_N^{600}) - J(\omega_N^{500})] - (13d^2/8)[J(0.955\omega_H^{600}) - \kappa J(0.955\omega_H^{500})]\} \qquad (7)$$

$$R_{ex} = R_2^{500} - [(d^2/2) + (2c^2_{500}/3)]J(0) - [(3d^2/8) + (2c^2_{500}/2)]J(\omega_N^{500}) - (13d^2/8)J(0.955\omega_H^{500}) \qquad (8)$$

where $\kappa = (\omega_H^{600}/\omega_H^{500})^2$, $\beta = (1 - \kappa)d^2/2$, and the subscripts and superscripts denote the frequency of the spectrometer at which the measurements were performed. The constants $d = (\mu_o h \gamma_H \gamma_N/8\pi^2)\langle r_{NH}^{-3}\rangle$ and $c_i = \omega_{Ni}\Delta\sigma/\sqrt{3}$, with μ_o being the permeability of free space, h Planck's constant, γ_H and γ_N the gyromagnetic ratios of the ^{1}H and ^{15}N nuclei, respectively, ω_{Ni} the Larmor frequencies of the ^{15}N spins at B_o = 11.7 T (500 MHz) or 14.1 T (600 MHz), r_{NH} the internuclear distance (1.02 Å), and $\Delta\sigma$ the chemical shift anisotropy of the ^{15}N spins. Heteronuclear NOEs at 500 MHz were recorded only once due to sensitivity limitations, and consequently, no error limits are given for the respective spectral density functions.

RESULTS

Overall Motion of CRABPI. The overall motions of the apo and holo forms of CRABPI at two different concentrations (0.2 and 1.2 mM) were measured by determination of the translational and rotational diffusion constants. Calculations based on the beads model approximation were used to further study the effect of concentration on the oligomeric state of the protein.

Nonlinear exponential fits to the experimental points generated by plotting the integrated area of the aliphatic region (4.25 to −1.25 ppm) of the spectra as a function the product of the area of gradient pulse strength and the diffusion length (eq 2, Materials and Methods, Figure 1) yielded self-diffusion coefficients (D_s^{expt}) (Table 1). The ratios of D_s^{expt} values at high and low concentrations (Table 1, last column) for apo and holo CRABPI are 0.70 and 0.73, respectively. A hard-sphere approximation model for dimer formation predicts a ratio of 0.731 for D_s(dimer)/D_s(monomer) (*50*, *51*), suggesting that to a good approximation, both apo and holo forms of CRABPI can self-associate (presumably forming dimers) at a concentration of 1.2 mM. The absolute values of self-diffusion coefficients of apo and holo CRABPI (14.87×10^{-11} and 16.64×10^{-11} m^2 s^{-1}, respectively, Table 1) are comparable to that of the monomeric form of a protein with a similar molecular mass (lysozyme, MW = 14.2 kDa, $D_s^{expt} = 13.36 \times 10^{-11}$ m^2 s^{-1}). Within the framework of self-diffusion coefficient measurement to determine protein oligomerization states, the results clearly show that both apo and holo CRABPI are

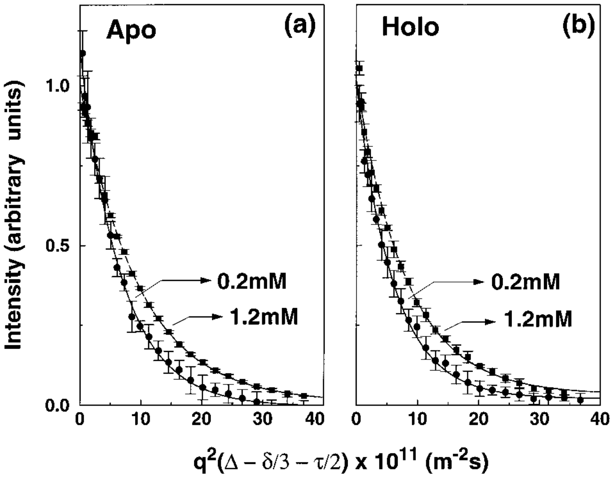

FIGURE 1: Plot of the self-diffusion coefficient measurements performed using BPP-SED for apo (a) and holo (b) CRABPI. Experimental points at the low (0.2 mM) and high (1.2 mM) concentrations are given by filled circles and squares, respectively, while the solid and dashed lines correspond to the fit to the diffusion curve. The error bars were obtained using triplicate experimental measurements.

predominantly monomeric at 0.2 mM, while at 1.2 mM, they tend to self-associate to form dimers.

Measurements of the laboratory frame relaxation rates (spin−lattice relaxation rate R_1 and spin−spin relaxation rate R_2) of the ^{15}N-labeled backbone nitrogens of apo and holo CRABPI at 0.2 and 1.2 mM (Table 2) were used to determine the overall rotational correlation times (*52*). The corresponding rotational correlation times (τ_c^{expt}) determined from trimmed (average values within one standard deviation) R_1/R_2 ratios at 0.2 and 1.2 mM and at field strengths of 500 and 600 MHz are listed in Table 2. In the case of the apo CRABPI, it was not possible to determine the τ_c^{expt} value at low concentrations as the variations in the R_2 values are too large to obtain an accurate trimmed ratio of R_2 to R_1. At 1.2 mM, τ_c^{expt} for the apo form is approximately 14 ns. In the case of holo CRABPI, the experimental τ_c values at low and high concentrations are 11 and 15 ns, respectively.

For a globular monomeric protein with a molecular mass similar to that of CRABPI (15.5 kDa), the expected rotational correlation time is around 6−8 ns. Several proteins of this size in the iLBP family have been studied, and they include I-FABP (MW = 14.82 kDa, τ_c = 6.7 ns) (*15*) and CRBPII (MW = 15.6 kDa, τ_c = 8.2 ns) (*53*). To better estimate the expected rotational correlation time (τ_c^{est}) based on the set of monomeric structures, an empirical correlation between rotational correlation time and solvent accessible surface area (SASA) was used (*32*) (Table 2). Accordingly, the τ_c^{est} for the monomeric form of apo CRABPI was 7.3 ns (experimental correlation) or 8.9 ns (theoretical correlation). The corresponding values for the holo protein are 6.8 and 8.4 ns, respectively (Table 2, last column). The SASA value of the holo protein is about 300 Å^2 lower than that of the apo protein, suggesting a smaller volume due to a tighter packing arrangement of the residues, and hence less flexibility (Table 2, footnote e). Although the differences between the τ_c^{expt} and τ_c^{est} do not arise from the anisotropic rotational motions of CRABPI (Table 2, footnote), they may come from other sources, such as the accuracy of the trimmed ratio of R_1 to R_2 and the presence of conformational exchange (*32*, *54*, *55*).

Hydrodynamic calculations using the beads model theory of Garcia de la Torre and Bloomfield (*30*, *31*) provided additional information about translational rotational motions of CRABPI. These calculations were based on the monomeric forms of the three-dimensional crystal structures of the apo (PDB entry 1cbi) and holo (PDB entry 1cbr) forms of CRABPI. As expected, the calculated self-diffusion coefficient (D_s^{calc}) values for both the apo and holo proteins are the comparable, since their structures are similar, but both are lower than the experimental values measured at 0.2 mM (Table 1, third column). Theoretical calculations of D_s^{calc} and τ_c^{calc} using the beads model (fourth column of Table 1 and fifth column of Table 2, respectively) typically represent values in the monomeric form and in the absence of hydration (*51*, *56*).

Residue Specific Motions of CRABPI. Assuming that the biologically active forms of both apo and holo proteins are more relevant at the low concentration (*11*, *26*), only the residue specific dynamics studies at 0.2 mM are presented here for both apo and holo CRABPI. The backbone amide ^{1}H and ^{15}N resonance assignments and secondary structures for apo (pH 7.5) and holo (pH 3.8) CRABPI were reported earlier (*14*). One hundred nineteen cross-peaks from apo CRABPI and 109 from the holo CRABPI are observed out of the 133 possible cross-peaks (excluding those from the three prolines). The assignments for the current study on the apo and holo forms at the same pH (7.5) were validated by additional ^{15}N-edited NOESY (nuclear Overhauser effect spectroscopy) and TOCSY (total correlation spectroscopy) experiments (*57*).

Intermediate Time Scale Motions, and Fast Amide Proton Exchange Rates. In general, motions occurring on a time scale faster than the conventional proton−deuterium replacement measurements or H−D exchange rates (k_{ex}^{HD}, 0.1−0.01 s^{-1}), but slower than the rotational correlation time (τ_c, ca. nanoseconds), can be defined as "intermediate time scale" motions. Rapid amide−proton exchange rates (k_{ex}^{HH}) of apo and holo CRABPI were measured using the ^{15}N-directed WEXII-FHSQC experiment proposed by Mori et al. (*33*). This experiment provides an excellent method of measuring k_{ex}^{HH} with the combined advantages of a well-defined mixing time, optimum control of water magnetization to avoid radiation damping, and minimal effects of water saturation.

The number of cross-peaks observed at short mixing times for the apo form is higher than that of the holo sample. The backbone amide proton exchange rates, as exemplified by the representative buildup curves for N14 (Figure 2a) and G47 (Figure 2b), are also faster for these specific residues in the apo form than in the holo form. Recently, several two-dimensional NMR experimental methods have been developed to provide accurate measurements of the rates of rapid transfer of water magnetization to protein amide protons (k_{ex}^{HH} ~ 0.1−100 s^{-1}) (*58*−*61*). These measurements allow the study of solvent-exposed amide protons, such as those that are close to or at the surface of the proteins. Plots summarizing the measured rapid amide exchange rates as a function of the residue number for the apo (Figure 3a) and holo (Figure 3b) CRABPI indicate that changes occur on this time scale in specific regions of the protein upon ligand binding (Figure 3c). Several residues in the well-defined secondary structure regions of the protein such as F15 and K20 in αI and M27, V31, and A35 in αII exhibit faster amide

Table 1: Overall Parameters of Translational Motion of Apo and Holo CRABPI

protein	concentration (mM)	D_s^{expt} ($\times 10^{-11}$ m^2 s^{-1})[a]	D_s^{calc} ($\times 10^{-11}$ m^2 s^{-1})[b]	D_{xx}:D_{yy}:D_{zz}[c]	$D_s^{1.2mM}/D_s^{0.2mM}$[d]
apo	0.2	14.87 ± 0.82	12.19	1.0:0.97:0.93	0.70
	1.2	10.43 ± 0.11			
holo	0.2	16.64 ± 0.86	12.45	1.0:0.97:0.92	0.73
	1.2	12.30 ± 0.31			

[a] Experimental self-diffusion coefficient measured using the BPP-SED sequence. Errors are estimated using triplicate measurements. [b] Calculated translational self-diffusion coefficient using the program DIFFC for all the backbone atoms with a scaling factor of 5 Å at 298 K in water, using the PDB (Protein Data Bank) coordinates of 1cbi and 1cbr for apo and holo CRABPI, respectively. [c] Ratios of the calculated translational diffusion tensor. [d] A ratio of 0.731 represents a dimer formation based on a hard-sphere approximation model (*51*).

Table 2: Overall Parameters of Rotational Motion of Apo and Holo CRABPI

protein	concentration (mM)	$\langle R_2/R_1\rangle_{av}$[a]	τ_c^{expt} (ns)	τ_c^{calc} (ns)[b]	τ_c^{est} (ns)[c]
apo[d]	0.2	6.44 ± 0.24	NA	7.64	7.26 ± 0.09 (c)
		10.30 ± 0.30			8.89 ± 0.23 (e)
	1.2	9.86 ± 0.16	14.89 ± 0.8		
		13.03 ± 0.2	13.33 ± 1.1		
holo[e]	0.2	7.27 ± 0.22	11.67 ± 1.1	7.13	6.8 ± 0.08 (c)
		10.28 ± 0.32	10.86 ± 0.66		8.42 ± 0.21 (e)
	1.2	13.34 ± 0.26	15.57 ± 0.57		
		13.80 ± 0.24	12.71 ± 0.59		

[a] Trimmed (average within one standard deviation) ratio of spin−spin to spin−lattice relaxation times at 500 (upper) and 600 MHz (lower). [b] Calculated rotational correlation time using the program DIFFC for all the backbone atoms with a scaling factor of 5 Å at 298 K in water, using the PDB (Protein Data Bank) coordinates of 1cbi and 1cbr for apo and holo CRABPI, respectively. [c] Estimated rotational correlation time using the empirical correlation between experimental values of τ_c and SASA (e) and calculated values of τ_c and SASA (c). [d] For apo CRABPI, the D_{xx}:D_{yy}:D_{zz} ratio was 0.81:0.89:1.0, where D_{ii} (*ii* being *xx*, *yy*, and *zz*) are the principal components of the calculated rotational diffusion tensor, and SASA = 7624.22 × 10^3 Å^2. [e] For holo CRABPI, the D_{xx}:D_{yy}:D_{zz} ratio was 0.76:0.85:1.0, where D_{ii} (*ii* being *xx*, *yy*, and *zz*) are the principal components of the calculated rotational diffusion tensor, and SASA = 7354.22 × 10^3 Å^2.

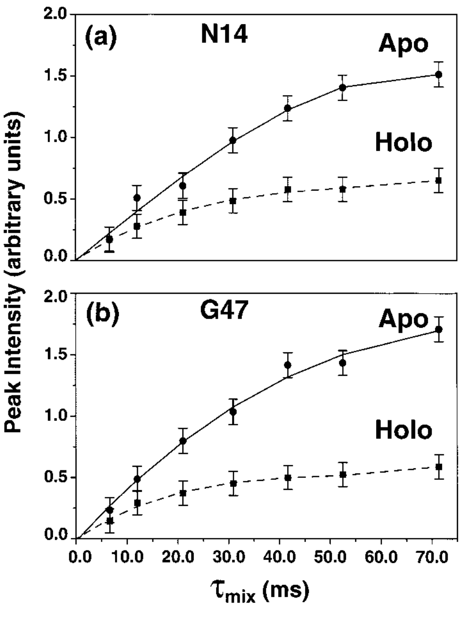

FIGURE 2: Normalized transfer of magnetization from water to amide protons in rapid amide exchange rate measurements as a function of mixing time, τ_{mix}, using WEXII-FHSQC for residues (a) N14 and (b) G47 in apo (●) and holo (■) CRABPI. The solid and the dashed lines are the corresponding fits to the experimental data as outlined in Materials and Methods. The error bars are obtained using duplicate measurements at specific mixing times.

proton exchange rates in the apo form than in the holo form. Such differences are further seen at the βB region of CRABPI, while significant changes seem to diminish in the other regions. In addition, amide protons are located in the flexible loop regions of the apo protein (for example, N14 in the βA_1−αI linker and D103 in the βG−βH turn). In particular, N14 shows one of the large differences in the amide exchange rate in the apo CRABPI ($k_{ex} = 22.7$ s^{-1}), which might signify a hinge motion of the βA_1−αI linker for ligand entry into the cavity. Several other amide protons in apo CRABPI (E62 and N64 in βC−βD and S83 in βE−βF) in the portal region (enclosed by αI, αII, and turns between βC−βD and βE−βF) also exhibit fast amide exchange rates. It is striking that in holo CRABPI, most of these residues do not undergo rapid amide exchange (Figure 3b). As both apo and holo CRABPI are predominantly monomeric at low concentrations as evidenced by the self-diffusion coefficient measurements, the difference seen in

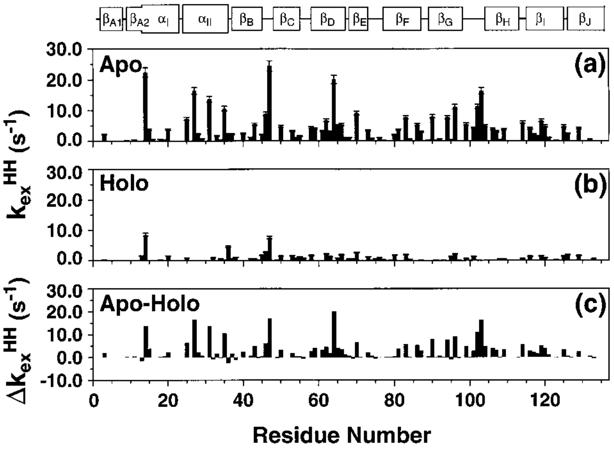

FIGURE 3: Measured rapid amide exchange rates (k_{ex}^{HH}) for apo (a) and holo (b) CRABPI as a function of the residue number in the amino acid sequence. The difference between exchange rates [$\Delta k_{ex}^{HH} = k_{ex}^{HH}$(apo) − k_{ex}^{HH}(holo)] is given in panel c. Error bars are obtained from the corresponding fits, and no error bars are given in the difference plot. The secondary structure of CRABPI is also represented at the top.

the rapid amide exchange rate measurements can be considered to arise primarily from the effect of ligand binding. These results provide direct experimental evidence that the retinoic acid recognition process proceeds through a dynamics-induced mechanism that involves slow motions of the portal region, which presumably make the internal binding cavity accessible for the ligand. It further indicates that the time scales of the motions that are important for ligand recognition are in the intermediate region, in the range of 10−30 s^{-1}.

The accuracy of k_{ex}^{HH} rate measurements depends on the other homonuclear cross-relaxation effects as the first water-selective pulse in the experiment may also excite other C^{α} protons that are close to the water frequency. Nonequilibrium magnetization from these C^{α} protons might subsequently transfer through NOE to the amide protons, which could mistakenly be identified as rapidly exchanging amide protons. Of the observed amide resonances of holo CRABPI, three of the residues (D46, A124, and V128) have their corresponding $C^{\alpha}H$ chemical shifts coincident with the water frequency. In addition, 14 other $C^{\alpha}H$ resonances (S11, R44, Q45, Q49, F50, I52, T54, T61, F65, E69, E73, R89, C95, and D126) fall within 0.1 ppm of the water resonance at 25 °C. Except for S11 (located at the beginning of β_{A2}) which shifts by 0.18 ppm toward lower field, none of the above-mentioned residues shift more than 0.1 ppm upon ligand binding. Since none of these residues show large values of rapid amide proton exchange rates in either apo or holo CRABPI, the influence of selective transfer of NOE from the $C^{\alpha}H$ protons in these measurements can be safely ignored. Recently, Mori et al. (*44*) have proposed a method for separating the exchange peaks from NOE peaks by means of a spin−echo filter prior to the water exchange (WEX) experiment. Although this method is effective in eliminating artifacts from NOE transfer, it was not possible to perform this experiment on our low-concentration samples due to low sensitivity. The upper limit of the k_{ex}^{HH} is governed by the pulse-interrupted free precession delay during the initial polarization transfer part of the pulse sequence, which is estimated to be approximately 100 s^{-1}, assuming an average nitrogen−proton coupling constant ($^{1}J_{NH}$) of 90 Hz. The lower limit is influenced by other cross-relaxation processes and can be approximated to be equivalent to the upper limit of the conventional k_{ex}^{HD} rate (0.1 s^{-1}).

Fast Time Scale Motions, and Laboratory Frame Relaxation Rate Measurements. The spin−lattice relaxation rate constant, R_1, the spin−spin relaxation rate constant, R_2, and the steady-state $\{^{1}H\}-^{15}N$ NOE were all obtained for the backbone ^{15}N nuclei by analysis of ^{1}H-detected two-dimensional $^{1}H-^{15}N$ heteronuclear single-quantum correlation (HSQC) spectra (*52*, *62*, *63*). The experimental values of R_1^{500}, R_2^{600}, and NOE^{500} are plotted versus residue number for the apo (left panels, a, c, and e) and holo (right panels, b, d, and f) forms of the protein in Figure 4. Although changes in the relaxation parameters on a residue-by-residue basis are potentially informative in comparing how these residues alter their dynamic behavior upon binding to retinoic acid, such differences are not significant enough here for further interpretation. As average values provide information about cooperative motions that might occur, Tables S1 and S2 (Supporting Information) list the average values of the various dynamic parameters over the NMR-identified secondary structural elements of apo and holo CRABPI, respectively. At 500 MHz, the values of R_1 for the apo and holo forms (1.78 ± 0.4 and 1.81 ± 0.20 s^{-1}, respectively) do not vary significantly as a function of sequence position. The corresponding values at 600 MHz are 1.59 ± 0.2 and 1.49 ± 0.14 s^{-1}, respectively. In general, the R_2 values for apo CRABPI are lower for most residues at 500 MHz than at 600 MHz, while the NOE values are higher at 500 MHz than at 600 MHz. In the case of holo CRABPI, several residues in the C-terminal segment and a few residues in the N-terminal region exhibit small variations in the R_2 values between 500 and 600 MHz, while the variations in the NOE between the 500 and 600 MHz data are not significant. Large variations in the R_2 values in both apo and holo CRABPI strongly suggest the presence of low-frequency motions, including possible conformation exchange on the microsecond to millisecond time scale region.

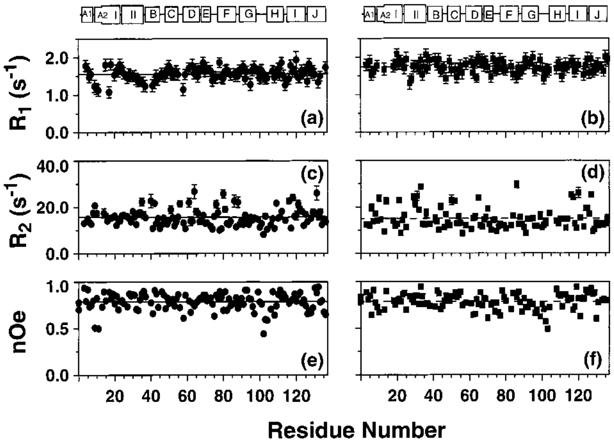

FIGURE 4: Representative examples of the relaxation parameters of apo (left panels) and holo (right panels) forms of CRABPI as a function of the residue number: (a) R_1^{500} (apo), (b) R_1^{500} (holo), (c) R_2^{600} (apo), (d) R_2^{600} (holo), (e) NOE^{500} (apo), and (f) NOE^{500} (holo). The secondary structure is shown at the top, with letters and roman numerals corresponding to the β-sheets and α-helices, respectively. Average values are also given by solid (apo form) and dotted (holo form) lines.

The model-free method of Lipari and Szabo (*64*) for the analysis of the laboratory frame relaxation rate measurements yielded unreliable overall and internal motional parameters for both apo and holo forms. The rotational anisotropy of the protein is not a reason for the failure as the ratio of the principal components of the rotational diffusion tensor is not highly anisotropic (Table 2) (*54*). In comparison to the model-free analysis of Lipari and Szabo, the reduced spectral density mapping method (*47*−*49*) gives a more simplified interpretation of experimental relaxation data without the requirement for a specific motional model (*62*). The analysis is independent of the rotational anisotropy of the protein and does not bias the estimated relaxation parameters if the system is undergoing a conformational exchange. Values of spectral density functions at three frequencies ($\omega = 0$, ω_N, and $0.87\omega_H$) were derived from the values of R_1, R_2, and NOE collected at 500 and 600 MHz (eqs 4−6, Materials and Methods). In general, the trends and variations in $J(0)$, $J(\omega_N)$, and $J(0.87\omega_H)$ are similar to the observed variations in R_2, R_1, and (1 − NOE), respectively (Tables S1 and S2). Although $J(0)$ is sensitive to motions that occur on both millisecond and microsecond time scales, it is not possible to separate these motions in a straightforward manner.

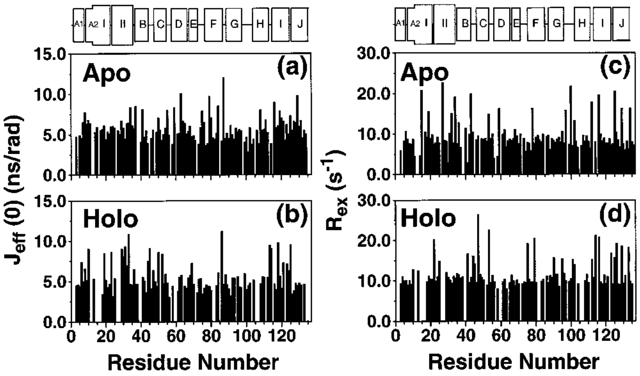

FIGURE 5: Effective spectral density close to zero frequency [$J_{eff}(0)$] contributions for the apo (a) and holo (b) CRABPI and conformational exchange (R_{ex}) contributions for the apo (c) and holo (d) forms as a function of the residue number estimated using reduced spectral density mapping at two spectrometer field strengths (500 and 600 MHz) along with the secondary structural elements shown at the top.

Alternatively, Farrow et al. (*49*) have shown that R_1, R_2, and NOE values obtained at two different field strengths can separate motions that occur close to zero frequency by effective spectral density close to zero frequency [$J_{eff}(0)$] and those of residues that undergo dominant conformational exchange by R_{ex} rates (eqs 7 and 8, Materials and Methods). Figure 5 shows the plots of $J_{eff}(0)$ (Figure 5a,c) and R_{ex} (Figure 5b,d) as a function of the residue number. At effective spectral density functions close to zero frequency, $J_{eff}(0)$ samples motions predominantly on the millisecond time scale as well as homonuclear cross-relaxation processes, which also occur at this frequency. The R_{ex} terms in the relaxation experiments sample motions on the microsecond time scale that might arise from conformational exchange. In the case of both apo and holo CRABPI, most residues undergo these types of motions, with moderate changes in $J_{eff}(0)$ found for the apo protein (Tables S1 and S2). In contrast to the rapid amide exchange rate measurements, slow time scale motions (milliseconds to microseconds) sampled by the multiple-field-dependent laboratory frame relaxation experiments do not show any residue specific differences. However, these results are important in separating the various time scales involved in the dynamics of CRABPI.

DISCUSSION

Protein Concentration Effects on Dynamics. Our detailed studies of CRABPI have revealed concentration-dependent effects on dynamics. Measurement of the overall motion of apo and holo CRABPI by self-diffusion coefficients and rotational correlation times (Tables 1 and 2) showed that an aggregation process is occurring as a function of increasing protein concentration. A decrease in the self-diffusion coefficient or an increase in the rotational correlation time signifies either of two phenomena: an increased solvent viscosity and an increase in the protein molecular mass. Self-diffusion coefficient measurements show that the effective diffusion constant of holo CRABP is higher than that of the apo form at the same concentration (Table 1, third column), suggesting that the increase in the diffusion constant cannot be attributed to lowering the solvent viscosity. Hence, self-diffusion coefficient measurements unequivocally show that apo and holo proteins undergo oligomerization (presumably dimerization) with increases in protein concentration. The results of the rotational correlation time measurements suggest that at low concentrations these proteins have a higher population of monomers, and no further investigations are performed due to the inherent uncertainties in the estimation. Nonetheless, the presence of a small amount of dimers or other oligomers may not be ruled out by the data; it might be possible to eliminate the presence of dimers altogether by further lowering the protein concentration. However, such protein concentrations are unlikely good conditions for detailed NMR study.

Measurements of backbone relaxation rates and rapid amide exchange rates for both the apo and holo CRABPI at a concentration of 1.2 mM were also performed (data not shown). No significant changes in the backbone relaxation parameters were observed upon increasing the concentration (from 0.2 to 1.2 mM) in either form, except for minor variation in the R_2 values. However, a noticeable reduction in the rapid amide proton exchange rates was observed only in the apo protein at the increased concentration, but the reduced exchange rates were still much larger than these in the holo protein at the same concentration. In addition, reduced spectral density mapping of the high-concentration data of both apo and holo CRABPI (data not presented) continues to show the presence of $J_{eff}(0)$ and R_{ex} terms.

When the protein concentration is increased from 0.2 to 1.2 mM, the observed changes in the amide proton or ^{15}N chemical shifts are not significant. Gabdoulline and Wade (*65*, *66*) have recently suggested that long-range electrostatic interactions between two monomers can influence the overall motional parameters such as rotational correlation time or self-diffusion coefficients, without stable van der Waals contacts between the monomers. In the case of CRABPI, however, it is not known whether electrostatic polarization of the charges that occur around the surface of CRABPI can aid the formation of dimers. Thus, the source for dimer formation is not clear under our experimental conditions. The physiologically relevant concentration of CRABPI is on the order of 2−5 μM (*67*), and it seems unlikely that the observed concentration-dependent dimer formation is relevant for its in vivo function. However, there are precedents that the formation of dimers may be important in how iLBPs function in the cell (*68*).

The crystal structure of apo CRABPI reveals the formation of an asymmetric dimer, in which the conformations of the monomeric units are not identical (*20*). The βD strands from each molecule formed five hydrogen bonds between them, to form a 20-stranded double β-barrel. Although it is not clear whether such structures exist in vivo, the earliest NMR studies of apo and holo forms of CRABPI also suggested that this protein self-associates, but only at a pH near the isoelectric point of 4.76 (*14*). A more recent solution structure study reported that at a concentration of 2 mM, CRABPII, which exhibits a high degree of sequence and structural homology with CRABPI, does not form a dimer (*25*). However, the evidence presented was indirect, such as a lack of NOEs between the monomers, rather than direct experimental measurements.

Oligomerization effects have been studied by NMR spectroscopy with increasing concentrations for several proteins (*55*, *69*−*73*). In most cases, however, these concentration effects directly manifest themselves in the mea-

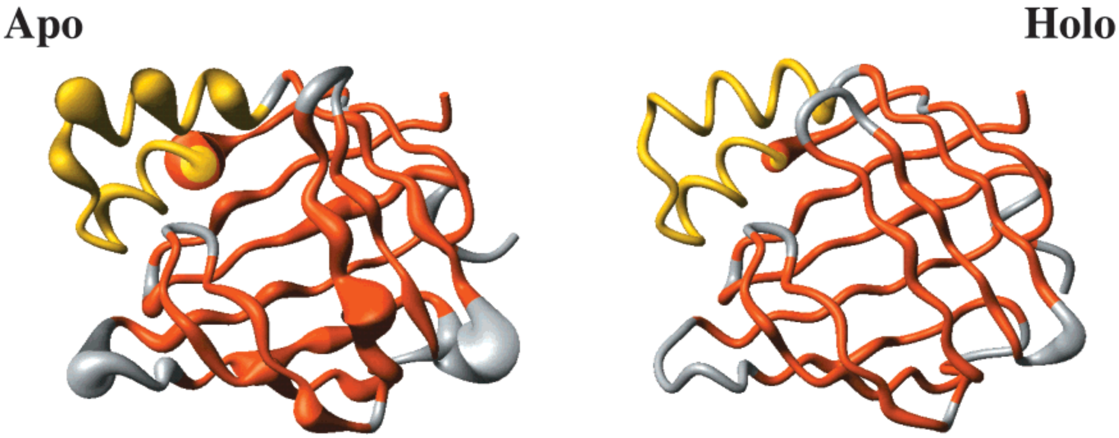

FIGURE 6: Schematic representation of the intermediate time scale motions that occur in apo (left) and holo (right) forms of cellular retinoic acid binding protein I (CRABPI). The rapid amide exchange rates (k_{ex}^{HH}) are superimposed onto the C^{α} traces of the crystal structure of apo (1cbi) and holo (1cbr) CRABPI. The magnitude of the motion is depicted as a tube with the radii proportional to the measured rapid amide exchange rates. The color codes of red, golden, and silver correspond to β-sheets, α-helices, and loops, respectively. The structure of the ligand is omitted in the holo CRABPI for the sake of clarity, and the figure was produced using MOLMOL (*80*).

sured NMR relaxation parameters such as line widths. For example, in the case of human cystatin (*69*), although self-diffusion coefficient measurements supported the presence of dimers, no monomer–dimer interconversion was observed. On the other hand, cold-shock protein A (*73*) shows a time-dependent formation of fibrils, but the conversion is slow enough to be monitored by a change in the ^{15}N line widths. The nature of a protein and the choice of experimental conditions, in some cases, have made it possible to characterize the monomers as well as dimers in solution (*71*, *72*).

Dynamical Changes upon Ligand Binding. The three-dimensional structures of the ligand-bound and free forms of proteins in the iLBP family do not show any significant differences, even at high resolution, although changes in stability are observed (*4*). Studies characterizing the dynamics of these proteins have provided indirect evidence, such as the absence of long-range homonuclear NOEs and small variations in the order parameter in the model-free analysis of Lipari and Szabo, for dynamics-induced ligand recognition and binding (*14*, *16*, *19*, *74*, *75*). However, the exact time scales of the motions that may be important determinants in ligand interactions were not determined. The dynamical measurements of CRABPI in its apo and holo forms presented here help to further define the time scales and nature of the motions that are important in how CRAPBI functions.

The extensive and systematic measurements of the relaxation rates at two spectrometer field strengths (R_1, R_2, and NOE at 500 and 600 MHz) and the subsequent analysis using reduced spectral density function analysis (eqs 4–8, Materials and Methods) show that there are no significant differences between the apo and holo forms of CRABPI at micro-, nano-, and picosecond time scales. The uniform presence of terms representing sub-microsecond time scale motions [$J_{eff}(0)$ and R_{ex}] suggests that there is some form of conformational exchange that is dominating the relaxation processes on these time scales.

Although there are no significant differences in the dynamics of apo and holo forms on most time scales, distinct motions that occur on the millisecond time scales were observed in apo CRABPI in the portal region (C-terminal portion of αII, the αII–βB linker, and the βC–βD and βE–βF turns) of apo CRABPI, and these motions were arrested upon retinoic acid binding. Previous measurements of exchange rates for the apo (pD 6.4 and 5 °C) and holo (pD 3.5 and 25 °C) forms using hydrogen–deuterium exchange experiments (*14*) have provided information that supports the dynamic portal model and about protein folding processes in CRABPI (*23*). Since these experiments could not provide information about the exchange rates of protons that are faster than the dead time of these experiments (typically, 2–5 min), saturation transfer experiments have been used to identify the rapidly exchanging amide protons well below 0.1 s^{-1} (*15*, *19*). These methods cannot accurately quantify exchange rates when unwanted spin diffusion effects are present in the measurements, which are inherently introduced by the required long saturation of water magnetization and also assume a uniform spin–lattice relaxation time (T_1) for all the amide protons. Thus, we have used the ^{15}N-directed WEXII-FHQC experiment to provide reliable measurements of the rapid exchange rates that occur on the millisecond time scale (*33*). In the case of CRABPI, these measurements have been important in identifying the exact time scale of the motions that change specifically upon ligand binding. However, to completely estimate the accuracy of these measurements, it is necessary to deuterate the aliphatic protons, and such an effort is underway in our laboratory. Nevertheless, the results we have obtained on the detailed dynamics of the apo and holo forms of CRABPI provide direct experimental evidence for the portal entry model, in which millisecond motions of the helix–turn–helix part of the apo protein allow the ligand entry into the binding pocket. These motions are arrested in the holo form, probably because of formation of stabilizing interactions between the ligand and the protein.

The schematic representation of the intermediate time scale motions as defined by the superposition of the observed values of k_{ex}^{HH} at 0.2 mM onto the three-dimensional X-ray structures of the apo and holo forms (Figure 6) graphically illustrates the regions in which the motions are arrested upon ligand binding. The radius of the tube representing the C^{α} trace of the molecule is proportional to the observed rapid amide exchange rates in the respective apo and holo forms.

The structure of holo CRABPI is presented without the retinoic acid for the sake of clarity. Although these results reveal the residues and the time scales involved in ligand binding processes, it is not yet possible to predict the exact roles of the various residues involved in these motions and the sequence of events that are important in ligand recognition. Future experiments on analogues with specific mutations in the helical region of the protein, which will either alter the electrostatic potential or arrest the motion or both, will better address the role of individual residues in ligand recognition and binding.

CONCLUSION

As noted by Laskowski et al. (*76*), only small differences are observed between the atomic resolution structures of many apo and holo proteins reported in the Protein Data Bank; typically, residues within a 5 Å radius of the ligand do not deviate more than 2 Å. Recently, efforts have been made to understand the subtle changes in conformational space due to ligand binding by careful analysis of changes introduced in surfaces, volumes, electrostatic potentials, and hydrophobic gradients (*77*−*79*). Although such efforts identify consistent changes (e.g., increased surface area and binding cavity volume upon ligand binding), the results are strictly based on the static or structural information of the proteins. NMR dynamic studies of proteins in the solution state provide an additional and powerful method for better understanding the differences between the apo and holo forms that are important in protein function.

Determination of self-diffusion rates shows that both apo and holo forms of CRABPI tend to self-associate and form higher-order aggregates such as dimers at higher concentrations (1.2 mM). Although there is no evidence that CRAPBI can exist as a dimer at the concentrations present in vivo, we cannot rule out the possibility that the concentration dependence of the oligomeric state of this protein may be important in regulation and ligand transfer processes.

Measurements of rapid amide proton exchange rates strongly indicate that several residues located in the helical regions of apo CRABPI undergo rapid amide exchange with water on the sub-millisecond time scale and that these motions are reduced significantly in holo CRABPI. These results not only further support the dynamic portal hypothesis but also suggest that the millisecond time scale motions in specific regions of the apo form may be important for ligand recognition and interaction.

ACKNOWLEDGMENT

We thank Drs. R. Balhorn (Lawrence Livermore National Laboratory) and K. Gunasekaran (University of Massachusetts) for critical reading of the manuscript and Joanna Feltham (University of Massachusetts) for help with Figure 6. We thank Professor Arseniev and co-workers (Russian Academy of Sciences, Moscow, Russia) for a copy of DIFFC and Dr. M. Akke (Lund University) for a copy of Felix macros.

SUPPORTING INFORMATION AVAILABLE

Apo and holo CRABPI dynamical parameters averaged over the various secondary structural elements. This material is available free of charge via the Internet at http://pubs.acs.org.

REFERENCES

1. Chytil, F., and Ong, D. E. (1987) *Annu. Rev. Nutr. 7*, 321−335.
2. Sweetser, D. A., Heuckeroth, R. O., and Gordon, J. I. (1987) *Annu. Rev. Nutr. 7*, 337−359.
3. Gordon, J. I., Sacchettini, J. C., Robson, I. J., Irieden, C., Li, E., Rubin, D. C., Roth, K. A., and Cistola, D. P. (1991) *Curr. Opin. Lipidol. 2*, 125−137.
4. Banaszak, L., Winter, N., Xu, Z., Bernlohr, D. A., Cowan, S., and Jones, T. A. (1994) *Adv. Protein Chem. 45*, 89−151.
5. Thompson, J., Ory, J., Reese-Wagoner, A., and Banaszak, L. (1999) *Mol. Cell. Biochem. 192*, 9−16.
6. Mansfield, S. G., Cammer, S., Alexander, S. C., Muehleisen, D. P., Gray, R. S., Tropsha, A., and Bollenbacher, W. E. (1998) *Proc. Natl. Acad. Sci. U.S.A. 95*, 6825−6830.
7. Bernlohr, D. A., Simpson, M. A., Hertzel, A. V., and Banaszak, L. J. (1997) *Annu. Rev. Nutr. 17*, 277−303.
8. Norris, A. W., Cheng, L., Giguere, V., Rosenberger, M., and Li, E. (1994) *Biochim. Biophys. Acta 1209*, 10−18.
9. Norris, A. W., Rong, D., Davignon, D. A., Rosenberger, M., Tasaki, K., and Li, E. (1995) *Biochemistry 34*, 15564−15573.
10. Wang, L. C., Li, Y., and Yan, H. G. (1997) *J. Biol. Chem. 272*, 1541−1547.
11. Napoli, J. L., Posch, K. P., Fiorella, P. D., and Boerman, M. (1991) *Biomed. Pharmacother. 45*, 131−143.
12. Maden, M., Ong, D. E., Summerbell, D., and Chytil, F. (1988) *Nature 335*, 733−735.
13. Sacchettini, J. C., Gordon, J. I., and Bananzak, L. J. (1989) *J. Mol. Biol. 208*, 327−339.
14. Rizo, J., Liu, Z. P., and Gierasch, L. M. (1994) *J. Biomol. NMR 4*, 741−760.
15. Hodsdon, M. E., and Cistola, D. P. (1997) *Biochemistry 36*, 2278−2290.
16. Hodsdon, M. E., and Cistola, D. P. (1997) *Biochemistry 36*, 1450−1460.
17. Zhang, J. H., Liu, Z. P., Jones, T. A., Gierasch, L. M., and Sambrook, J. F. (1992) *Proteins: Struct., Funct., Genet. 13*, 87−99.
18. Chen, X., Tordova, M., Gilliland, G. L., Wang, L. C., Li, Y., Yan, H. G., and Ji, X. H. (1998) *J. Mol. Biol. 278*, 641−653.
19. Wang, L. C., and Yan, H. G. (1998) *Biochemistry 37*, 13021−13032.
20. Thompson, J. R., Bratt, J. M., and Banaszak, L. J. (1995) *J. Mol. Biol. 252*, 433−446.
21. Wang, L., and Yan, H. (1999) *Biochim. Biophys. Acta 1433*, 240−252.
22. Kleywegt, G. J., Bergfors, T., Senn, H., Lemotte, P., Gsell, B., Shudo, K., and Jones, T. A. (1994) *Structure 2*, 1241−1258.
23. Clark, P. L., Liu, Z. P., Rizo, J., and Gierasch, L. M. (1997) *Nat. Struct. Biol. 4*, 883−886.
24. Schroeder, F., Jolly, C. A., Cho, T. H., and Frolov, A. (1998) *Chem. Phys. Lipids 92*, 1−25.
25. Wang, L. C., Li, Y., Abildgaard, F., Markley, J. L., and Yan, H. G. (1998) *Biochemistry 37*, 12727−12736.
26. Dong, D., Ruuska, S. E., Levinthal, D. J., and Noy, N. (1999) *J. Biol. Chem. 274*, 23695−23698.
27. Wu, D. H., Chen, A. D., and Johnson, C. S., Jr. (1995) *J. Magn. Reson., Ser. A 115*, 260−264.
28. Krishnan, V. V., Thornton, K. H., and Cosman, M. (1999) *Chem. Phys. Lett. 302*, 317−323.
29. Mescher, M., Tannus, A., Johnson, M. O., and Garwood, M. (1996) *J. Magn. Reson., Ser. A 123*, 226−229.
30. Garcia de la Torre, J. G., and Bloomfield, V. A. (1981) *Q. Rev. Biophys. 14*, 81−139.
31. Orekhov, V. Y., Nolde, D. E., Golovanov, A. P., Korzhnev, D. M., and Arseniev, A. S. (1995) *Appl. Magn. Reson. 9*, 581−588.
32. Krishnan, V. V., and Cosman, M. (1998) *J. Biomol. NMR 12*, 177−182.
33. Mori, S., Abeygunawardana, C., Berg, J. M., and vanZijl, P. C. M. (1997) *J. Am. Chem. Soc. 119*, 6844−6852.
34. Shaka, A. J., Barker, P. B., and Freeman, R. (1985) *J. Magn. Reson. 64*, 547−552.

35. Farrow, N. A., Muhandiram, R., Singer, A. U., Pascal, S. M., Kay, C. M., Gish, G., Shoelson, S. E., Pawson, T., Formankay, J. D., and Kay, L. E. (1994) *Biochemistry 33*, 5984−6003.
36. Farrow, N. A., Zhang, O. W., Formankay, J. D., and Kay, L. E. (1995) *Biochemistry 34*, 868−878.
37. Kay, L. E., Keifer, P., and Saarinen, T. (1992) *J. Am. Chem. Soc. 114*, 10663−10665.
38. Shaka, A. J., Keller, J., Frenkiel, T., and Freeman, R. (1983) *J. Magn. Reson. 52*, 335−338.
39. Markley, J. L., Horsley, W. J., and Klein, M. P. (1971) *J. Chem. Phys. 55*, 3604−3605.
40. Jones, J. A., Hodgkinson, P., Barker, A. L., and Hore, P. J. (1996) *J. Magn. Reson., Ser. B 113*, 25−34.
41. Jones, J. A. (1997) *J. Magn. Reson. 126*, 283−286.
42. Delaglio, F., Grzesiek, S., Vuister, G. W., Zhu, G., Pfeifer, J., and Bax, A. (1995) *J. Biomol. NMR 6*, 277−293.
43. Johnson, B. A., and Blevins, R. A. (1994) *J. Biomol. NMR 4*, 603−614.
44. Mori, S., Berg, J. M., and Vanzijl, P. C. M. (1996) *J. Biomol. NMR 7*, 77−82.
45. Abragam, A. (1961) *The principles of nuclear magnetism*, Chapter VIII, Clarendon Press, Oxford, U.K.
46. Noggle, J. H., and Schirmer, R. E. (1971) *The nuclear Overhauser effect; chemical applications*, Chapter 1−3, Academic Press, New York.
47. Peng, J. W., and Wagner, G. (1992) *J. Magn. Reson. 98*, 308−332.
48. Ishima, R., and Nagayama, K. (1995) *Biochemistry 34*, 3162−3171.
49. Farrow, N. A., Zhang, O. W., Szabo, A., Torchia, D. A., and Kay, L. E. (1995) *J. Biomol. NMR 6*, 153−162.
50. Teller, D. C., Swanson, E., and de Haën, C. (1979) *Methods Enzymol. 61*, 103−124.
51. Krishnan, V. V. (1997) *J. Magn. Reson. 124*, 468−473.
52. Clore, G. M., Driscoll, P. C., Wingfield, P. T., and Gronenborn, A. M. (1990) *Biochemistry 29*, 7387−7401.
53. Lu, J. Y., Lin, C. L., Tang, C. G., Ponder, J. W., Kao, J. L. F., Cistola, D. P., and Li, E. (1999) *J. Mol. Biol. 286*, 1179−1195.
54. Schurr, J. M., Babcock, H. P., and Fujimoto, B. S. (1994) *J. Magn. Reson., Ser. B 105*, 211−224.
55. Fushman, D., Cahill, S., and Cowburn, D. (1997) *J. Mol. Biol. 266*, 173−194.
56. Squire, P. G., and Himmel, M. E. (1979) *Arch. Biochem. Biophys. 196*, 165−177.
57. Marion, D., Driscoll, P. C., Kay, L. E., Wingfield, P. T., Bax, A., Gronenborn, A. M., and Clore, G. M. (1989) *Biochemistry 28*, 6150−6156.
58. Gemmecker, G., Jahnke, W., and Kessler, H. (1993) *J. Am. Chem. Soc. 115*, 11620−11621.
59. Kriwacki, R. W., Hill, R. B., Flanagan, J. M., Caradonna, J. P., and Prestegard, J. H. (1993) *J. Am. Chem. Soc. 115*, 8907−8911.
60. Andrec, M., Hill, R. B., and Prestegard, J. H. (1995) *Protein Sci. 4*, 983−993.
61. Koide, S., Jahnke, W., and Wright, P. E. (1995) *J. Biomol. NMR 6*, 306−312.
62. Dayie, K. T., Wagner, G., and Lefèvre, J. F. (1996) *Annu. Rev. Phys. Chem. 47*, 243−282.
63. Palmer, A. G. (1997) *Curr. Opin. Struct. Biol. 7*, 732−737.
64. Lipari, G., and Szabo, A. (1982) *J. Am. Chem. Soc. 104*, 4546−4559−4570.
65. Gabdoulline, R. R., and Wade, R. C. (1997) *Biophys. J. 72*, 1917−1929.
66. Gabdoulline, R. R., and Wade, R. C. (1998) *Methods Enzymol. 14*, 329−341.
67. Napoli, J. L. (1997) *Semin. Cell Dev. Biol. 8*, 403−415.
68. Thompson, J., Winter, N., Terwey, D., Bratt, J., and Banaszak, L. (1997) *J. Biol. Chem. 272*, 7140−7150.
69. Ekiel, I., Abrahamson, M., Fulton, D. B., Lindahl, P., Storer, A. C., Levadoux, W., Lafrance, M., Labelle, S., Pomerleau, Y., Groleau, D., LeSauteur, L., and Gehring, K. (1997) *J. Mol. Biol. 271*, 266−277.
70. Gryk, M. R., Abseher, R., Simon, B., Nilges, M., and Oschkinat, H. (1998) *J. Mol. Biol. 280*, 879−896.
71. Pfuhl, M., Chen, H. A., Kristensen, S. M., and Driscoll, P. C. (1999) *J. Biomol. NMR 14*, 307−320.
72. Crump, M. P., Spyracopoulos, L., Lavigne, P., Kim, K. S., Clark-Lewis, I., and Sykes, B. D. (1999) *Protein Sci. 8*, 2041−2054.
73. Alexandrescu, A. T., and Rathgeb-Szabo, K. (1999) *J. Mol. Biol. 291*, 1191−1206.
74. Lücke, C., Fushman, D., Ludwig, C., Hamilton, J. A., Sacchettini, J. C., and Rüterjans, H. (1999) *Mol. Cell. Biochem. 192*, 109−121.
75. Li, E. (1999) *Mol. Cell. Biochem. 192*, 105−108.
76. Laskowski, R. A., Luscombe, N. M., Swindells, M. B., and Thornton, J. M. (1996) *Protein Sci. 5*, 2438−2452.
77. Colombo, M. F., Rau, D. C., and Parsegian, V. A. (1992) *Science 256*, 655−659.
78. Liang, J., Edelsbrunner, H., and Woodward, C. (1998) *Protein Sci. 7*, 1884−1897.
79. LiCata, V. J., and Bernlohr, D. A. (1998) *Proteins: Struct., Funct., Genet. 33*, 577−589.
80. Koradi, R., Billeter, M., and Wüthrich, K. (1996) *J. Mol. Graphics 14*, 51−55.

BI000296L